Journal of Quantitative Spectroscopy & Radiative Transfer 189 (2017) 168–175

Contents lists available at ScienceDirect

Journal of Quantitative Spectroscopy & Radiative Transfer

journal homepage: www.elsevier.com/locate/jqsrt

Multi-wavelength UV-detection in capillary hydrodynamic fractionation. Data treatment for an absolute estimate of the particle size distribution

Luis A. Clementi [a,b], Miren Aguirre [c], José R. Leiza [c], Luis M. Gugliotta [a], Jorge R. Vega [a,b,*]

[a] INTEC (CONICET and Universidad Nacional del Litoral), Güemes 3450, 3000 Santa Fe, Argentina
[b] FRSF-UTN (Facultad Regional Santa Fe – Universidad Tecnológica Nacional), Lavaisse 610, 3000 Santa Fe, Argentina
[c] POLYMAT, University of the Basque Country (UPV/EHU), Joxe Mari Korta Center, Avenida Tolosa 72, 20018 Donostia-San Sebastián, Spain

ARTICLE INFO

Article history:
Received 31 July 2016
Received in revised form
25 November 2016
Accepted 25 November 2016
Available online 27 November 2016

Keywords:
Particle size distribution
Capillary hydrodynamic fractionation
Multi-wavelength UV-detection
Instrumental broadening

ABSTRACT

A new approach is proposed for estimating the particle size distribution (PSD) of hydrophobic colloids by capillary hydrodynamic fractionation (CHDF) based on UV-detection at several wavelengths. At each elution time, the multi-wavelength UV signal is used to estimate the instantaneous PSD at the detector cell by solving the involved inverse problem through an artificial neural network. Then, the global PSD is obtained as a weighted sum of the estimated instantaneous PSDs along the entire elution time interval. With the current approach, the estimation procedure is absolute in the sense that no calibration of diameters is required and the instrumental broadening introduced by the fractionation capillary is automatically compensated for. The proposed method was evaluated on the basis of narrow polystyrene standards, as follows: i) a single standard, to emulate a narrow unimodal PSD; ii) a mixture of three standards of relatively close average diameters, to emulate a broad unimodal PSD; and iii) a mixture of two standards of quite different average diameters, to emulate a bimodal PSD. Experimental results indicate that the new approach is able to produce adequate PSD estimates provided that the particle refractive index is known with a relatively high accuracy.

1. Introduction

The particle size distribution (PSD) is a key variable of particulate colloids that influences important properties such as the rheological behavior, the chemical stability, the coagulation processes, and the diffusion rates. In the case of polymeric colloids (or latexes) the PSD estimation is of primary importance not only for quality control, but also for the study of some physico-chemical mechanisms (such as nucleation, growth, and interaction of polymer particles) that take place along the polymerization reactions [1].

The ordinates of the discrete number PSD, $f(D_n)$, represent the number fraction of particles contained in the diameter interval $[D_n-\Delta D/2, D_n+\Delta D/2]$ ($n = 1, \ldots, N$), being ΔD a regular partition of the diameter axis; then: $\sum_{n=1}^{N} f(D_n) = 1$. Main definitions concerning PSDs of homogeneous spherical particles have been reviewed in Gugliotta et al. [1].

Several techniques are available for estimating the PSD of particulate colloids [1]. Light scattering techniques such as dynamic light scattering (DLS) [1–7], multiangle static light scattering (SLS) [1,7–9], and Turbidity (T) [1,10–14] are fast, repetitive, and inexpensive; and also absolute in the sense that they do not require a diameter calibration. Unfortunately, these techniques require the knowledge of the particle refractive index (PRI) at the utilized wavelengths and are based on the solution of an ill-conditioned inverse problem [15] that can produce erroneous PSDs estimates due to the unavoidable presence of measurement noises [1]. Moreover, in general, light scattering techniques produce PSDs with acceptable average diameters but overestimated widths due to the regularization method used for solving the involved ill-conditioned inverse problem [1,10,11,13,15].

Appendix A presents the mathematical model for T measurements. The main application of this technique has been related to the detection of particle concentration in fractionation techniques that utilize a single-wavelength UV sensor (such as, capillary hydrodynamic fractionation: CHDF, disc centrifuge photodensitometry: DCP, field flow fractionation: FFF, and hydrodynamic chromatography: HDC). In contrast, multi-wavelength T measurements have been widely utilized for estimating PSDs in

* Corresponding author at: INTEC (CONICET and Universidad Nacional del Litoral), Güemes 3450, 3000 Santa Fe, Argentina.
E-mail addresses: laclementi@santafe-conicet.gov.ar (L.A. Clementi), miren.aguirre@ehu.eus (M. Aguirre), jrleiza@ehu.eus (J.R. Leiza), lgug@intec.unl.edu.ar (L.M. Gugliotta), jvega@santafe-conicet.gov.ar (J.R. Vega).

http://dx.doi.org/10.1016/j.jqsrt.2016.11.024
0022-4073/

hydrophobic colloids [1,10–14]. For example, Eliçabe and Garcia-Rubio [10] utilized a regularization technique for estimating the PSD of polystyrene latexes from T measurements at wavelengths in the range [200–900 nm]. Based on simulated examples, the regularization technique was able to acceptably estimate unimodal and bimodal PSDs. Llosent et al. [12] successfully estimate the PSD of industrial styrene-butadiene rubber (SBR) and acrylonitrile-butadiene rubber (NBR) latexes from T measurements at wavelengths in the range [300–600 nm]. In their work, a previous independent estimation of the PRI at the employed wavelengths range was required, and even though the PSDs were narrow and involved small particles (near the Rayleigh region) their estimates were close to those obtained by SEM. Also, Gugliotta et al. [1] estimated the PSD of a pressure sensitive adhesive through T measurements, and verified that uncertainties in the PRI can produce meaningful differences in the estimated PSDs.

On the other hand, fractionation techniques such as CHDF are fast and require a relatively simple and straightforward data treatment for estimating the PSD of particulate colloids [16,17]. In CHDF, the particles are separated along a capillary tube according to their sizes. In fact, the particles, dragged by the carrier fluid, exhibit a parabolic velocity profile with null velocity at the capillary wall and maximum velocity at the center of the capillary. Due to the pseudo-random movement across the capillary, a particle of diameter D can only experience the carrier velocities corresponding to a reduced cross-sectional area that excludes the layer of thickness $D/2$ adjacent to the capillary wall. Thus, a small particle, which is affected by a thin exclusion layer, will be dragged to the low velocities adjacent to the capillary wall. In contrast, a large particle is affected by a wider exclusion layer and will be dragged to a higher velocity. In consequence, smaller particles will move slower than larger particles, and therefore a fractionation according to particle sizes will be obtained along the capillary [16,17].

The estimation of the PSD of a colloid by standard CHDF involves the following steps: i) to inject the diluted sample into the fractionation capillary; ii) to inject the marker solution (e.g., sodium dichromate), approximately 60∼120 seconds later than the sample injection; iii) to measure the fractogram, $\tau(t_i)$, through T at a single detection wavelength, λ_0, and at the discrete elution times, t_i ($i=1, \ldots, I$); iv) to calculate the fractogram, $\tau_R(R_i)$, where R_i ($= t_m/t_i$) is the relative elution time and t_m is the elution time associated with the apex of the fractogram corresponding to the marker solution; and v) to calculate the PSD, $f(D_n)$, through the procedure described in Appendix B.

The main advantages of CHDF are: i) the PSD estimates are obtained in a relatively short time (ca. 10∼20 minutes, depending on the utilized fractionation capillary); ii) high efficiency for identifying multiple modes in multimodal PSDs; and iii) easy to use even for non-trained users. However, the technique exhibits important drawbacks: i) a diameter calibration is required; ii) the PRI must be known; and iii) instrumental broadening (IB) must be corrected for. Due to IB, a complete PSD is present in the detection cell (instead of a particle population of equal diameters). Without IB correction, PSDs of overestimated widths are obtained; and narrow distributions are affected by high errors. A review on the CHDF technique, the involved data treatment, and its main drawbacks is currently available [18].

CHDF has been utilized for sizing colloids in several applications [17,19–28]. For example, DosRamos and Silebi [17] used CHDF for characterizing latex of multimodal PSDs, obtained by blending several PS narrow standards. Compared to TEM estimates, CHDF successfully recovered the shapes of all PSDs, although some appreciable differences were observed in the average diameters of each estimated mode. On the other hand, Elizalde et al. [21] analyzed PS latexes and compared the performance of DCP, CHDF, and DLS for estimating the PSD of the samples. The techniques were assessed in terms of the determination of the two or three present modes, the accuracy of the average diameter of the peaks and the number concentration of each mode as compared with the known amounts used in their preparation. Experimental results showed that CHDF and DCP produced similar and acceptable PSD estimates, although in all cases the peaks obtained by CHDF exhibited an overestimated width. Miller et al. [19], Erdem et al. [22], and Casey et al. [27] used CHDF for monitoring the droplet size distribution evolution in miniemulsions. Also, Miller et al. [20] used CHDF as a tool for monitoring the PSD of a PS latex along a miniemulsion polymerization reaction. The obtained PSDs were in good agreement with estimations obtained by TEM. Similarly, Jung and Shul [23] employed CHDF for estimating the PSD of zeolite particles during crystallization reactions, and compared their results to those obtained by TEM and SEM. More recently, Mariz et al. [24–26] utilized CHDF for monitoring the evolution of the PSD during the seeded semibatch emulsion polymerization of methyl methacrylate, butyl acrylate, and acrylic acid (MMA/BA/MAA). The goal of the polymerization reaction was to produce latexes of high solids content with low viscosity. In order to achieve this objective, a polymerization strategy was designed to produce a bimodal latex with well defined particle size and number concentration of each mode. Results showed that PRI uncertainties could produce meaningful deviations in the estimated PSDs. In general, an erroneous PRI produces acceptable average particle size values for each mode but the number concentration of each mode is highly erroneous [18]. Recently, Picchio et al. [28] utilized CHDF for monitoring the nucleation process in a batch emulsion polymerization of methyl methacrylate in the presence of varied concentration of casein. In that work, the PSDs estimated by CHDF were fundamental to elucidate the nucleation mechanisms that took place along the polymerization reaction.

In this work, a novel method is proposed for estimating the PSD of hydrophobic colloids by CHDF, which is based on a multi-wavelength T detection. The new approach involves solving an inverse problem at each discrete elution time for estimating the instantaneous PSD at the detector cell. Finally, the global PSD is estimated by a weighted sum of the instantaneous PSDs along the entire elution time range. The method is evaluated on the basis of PS samples that exhibit unimodal (narrow and broad) and bimodal PSDs, and the results are compared to those obtained by DLS and standard CHDF.

2. The proposed method

Consider a CHDF experiment with simultaneous measurements at several wavelengths λ_j ($j=1,\ldots, J$). The corresponding bivariate fractogram is expressed as $\tau(t_i, \lambda_j)$ ($i = 1, \ldots, I, j = 1, \ldots, J$). At a fixed elution time t_{i*}, $\tau(t_{i*}, \lambda_j) = \tau_{i*}(\lambda_j)$ represents a T measurement. Then, Equation (A.2) can be numerically inverted to obtain the estimated instantaneous PSD, $\hat{f}_{i*}(D_n)$, i.e. the estimation of the PSD that is present in the detector cell at each t_{i*}.

From $\hat{f}_{i*}(D_n)$, the estimated particle number concentration at the detector cell at time t_{i*}, $\hat{c}(t_{i*})$, can be also calculated by solving Eq. (A.2) at any λ_j, i.e.:

$$\hat{c}(t_{i*}) = \frac{\tau_{i*}(\lambda_j)}{(\pi/4)\ \sum_{n=1}^{N} Q_{ext}[D_n, \lambda_0, n_m(\lambda_j), n_p(\lambda_j)]\ D_n^2\ \hat{f}_{i*}(D_n)} \quad (1)$$

Finally, from $\hat{f}_{i*}(D_n)$ and $\hat{c}(t_{i*})$, the estimated global PSD, $\hat{f}(D_n)$, is calculated as:

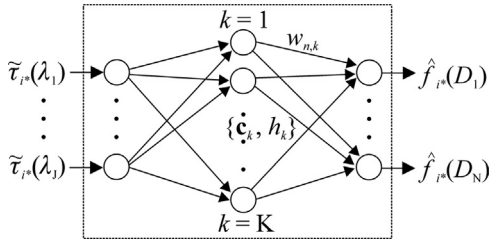

Fig. 1. Schematic representation of the utilized GRNN.

$$\hat{f}(D_n) = \frac{\sum_{i^*=1}^{I} \hat{c}(t_{i*}) \hat{f}_{i*}(D_n)}{C_T} \tag{2}$$

where $C_T = \sum_{i*=1}^{I} \hat{c}(t_{i*})$ is the total concentration. In what follows, an inversion method based on neural networks is proposed for estimating the instantaneous PSDs, $\hat{f}_{i*}(D_n)$.

2.1. Solution of the inverse problem through a general regression neural network

Consider the problem of inverting Eq. (A.2) for estimating the instantaneous PSDs, $\hat{f}_{i*}(D_n)$ ($i^* = 1, \ldots, I$; $n = 1, \ldots, N$), on the basis of a multi-wavelength T measurement, $\tau_{i*}(\lambda_j)$ ($j = 1, \ldots, J$). Fig. 1 shows a schematic representation of the general regression neural network (GRNN) with a single hidden layer of K neurons, which is utilized for solving the described inverse problem [29]. Such GRNN receives J inputs (the J ordinates of the normalized T measurement $\tilde{\tau}_{i*}(\lambda_j) = \tau_{i*}(\lambda_j)/\tau_{i*}(\lambda_1)$); and produces N outputs (the N ordinates of $\hat{f}_{i*}(D_n)$). Input and output information can be arranged in two column vectors, the input vector $\tilde{\boldsymbol{\tau}} = [\tilde{\tau}_{i*}(\lambda_1), \cdots, \tilde{\tau}_{i*}(\lambda_J)]' = [\tau_{i*}(\lambda_1)/\tau_{i*}(\lambda_1), \cdots, \tau_{i*}(\lambda_J)/\tau_{i*}(\lambda_1)]'$ and the output vector $\hat{\mathbf{f}} = [\hat{f}_{i*}(D_1), \cdots, \hat{f}_{i*}(D_N)]'$, where $[\cdots]'$ indicates transpose vector. The k-th neuron in the hidden layer produces a scalar output of amplitude h_k, given by:

$$h_k = \frac{1}{s_k\sqrt{2\pi}} \, e^{-\frac{\| \tilde{\boldsymbol{\tau}} - \mathbf{c}_k \|^2}{2 s_k^2}}; \; (k = 1, \ldots, K) \tag{3}$$

where $\| \tilde{\boldsymbol{\tau}} - \mathbf{c}_k \|$ represents the Euclidean distance between the input vector $\tilde{\boldsymbol{\tau}}$ and the center $\mathbf{c}_k$ ($J \times 1$) of the k-th neuron in the hidden layer; and s_k is the so-called smoothness parameter associated with the k-th neuron. From h_k, the output $\hat{f}_{i*}(D_n)$ of the GRNN is calculated as follows:

$$\hat{f}_{i*}(D_n) = \sum_{k=1}^{K} w_{n,k} \; h_k; \; (n = 1, \ldots, N) \tag{4}$$

where $w_{n,k}$ is the weight coefficient of the connection between the k-th hidden neuron and the n-th output neuron. The center of each hidden neuron $\mathbf{c}_k$ and the weight of their connections with the output layer $\mathbf{w}_k = (w_{1,k}, \cdots, w_{N,k})$ are chosen by the training procedure that is described in the following section.

2.2. Training the neural network

The training procedure of a GRNN is fast and simple [30]. To this effect, a set of K_t pairs $\{ \tilde{\boldsymbol{\tau}}_k = [\tilde{\tau}_k(\lambda_1), \cdots, \tilde{\tau}_k(\lambda_J)]', \mathbf{f}_k = [f_k(D_1), \cdots, f_k(D_N)]' \}$ ($k = 1, \ldots, K_t$) (the training patterns) is presented to the GRNN. A subset of $K < K_t$ randomly chosen training patterns is utilized for determining the values of $\mathbf{c}_k$ and $\mathbf{w}_k$. Note that the number of hidden neurons, K, coincides with the number of training patterns. The center of the k-th hidden neuron is chosen as $\mathbf{c}_k = \tilde{\boldsymbol{\tau}}_k$, and the weight coefficients of the connections with the output layer are chosen as $\mathbf{w}_k = \mathbf{f}_k$. Consequently, from Eq. (4), the output of the GRNN produces the following PSD estimate:

$$\hat{f}_{i*}(D_n) = \sum_{k=1}^{K} h_k \; f_k(D_n) \tag{5}$$

with

$$h_k = \frac{1}{s_k\sqrt{2\pi}} \, e^{-\frac{\| \tilde{\boldsymbol{\tau}} - \tilde{\boldsymbol{\tau}}_k \|^2}{2 s_k^2}} \tag{6}$$

According to Eq. (5), the output of the GRNN is obtained as the linear combination of the training patterns $f_k(D_n)$ weighted by the coefficients h_k ($k = 1, \ldots, K$). Such coefficients become larger when the centers $\mathbf{c}_k = \tilde{\boldsymbol{\tau}}_k$ are closer to the input $\tilde{\boldsymbol{\tau}}$. Thus, the output of the GRNN is mostly defined by those training patterns $f_k(D_n)$ that exhibit a small distance $\|\tilde{\boldsymbol{\tau}} - \mathbf{c}_k\| = \|\tilde{\boldsymbol{\tau}} - \tilde{\boldsymbol{\tau}}_k\|$.

The smoothness parameter s_k affects the selectivity of each hidden neuron. A small s_k typically produces a highly selective GRNN; i.e., only those neurons that have a small norm $\| \tilde{\boldsymbol{\tau}} - \tilde{\boldsymbol{\tau}}_k \|$ will meaningfully contribute to the output. On the contrary, a high s_k produces a less selective GRNN, and therefore neurons with larger distances $\| \tilde{\boldsymbol{\tau}} - \tilde{\boldsymbol{\tau}}_k \|$ will also contribute to the output. Therefore, low values of s_k can lead to estimates that exhibit several spurious peaks. In contrast, high values of s_k will produce smoother (but probably distorted) estimates. The optimal smoothness parameter s_k can be chosen according to the "Holdout" method proposed by Specht [30]. To this effect, all $K^* = K_t - K$ patterns that were not used in the selection of $\mathbf{c}_k$ and $\mathbf{w}_k$ are utilized for determining s_k, by solving the following optimization problem:

$$\min_{s_k} \left(\sum_{k=1}^{K^*} \| \mathbf{f}_k - \hat{\mathbf{f}}_k \| \right) \tag{7}$$

where $\hat{\mathbf{f}}_k$ is the PSD estimated by the GRNN for $\mathbf{f}_k$. According to the "Holdout" method, s_k is chosen as the value that best reproduces the PSD of the K^* patterns. This method presents the advantage of its simple implementation and automation.

3. Experimental work

A CHDF-3000 (from Matec Applied Sciences), fitted with a multi-diode array detector that allows the simultaneous detection at four chosen wavelengths, was utilized. At the low sample concentrations utilized in CHDF, acceptable signal-to-noise ratios are only obtained at the UV range; and for this reason, all measurements were made at the following wavelengths: 220 nm, 240 nm, 260 nm, and 280 nm; while the wavelength resolution of the multi-diode array is 1 nm. Table 1 shows the specifications of all polystyrene (PS) NIST traceable size standards utilized for

Table 1
Nominal and average diameters, D_{nom} [nm] and $\bar{D}$ [nm], respectively, and standard deviation, σ [nm], of the employed polystyrene NIST calibration standards as provided by the manufacturer: Polysciences Inc. ($\bar{D}$ and σ were estimated by DCP according to the manufacturer).

D_{nom}	$\bar{D}$	σ
50	51	7.3
80	86	5.9
150	150	8.9
200	206	6.3
250	244	8.9
300	286	19.5
350	356	14.0

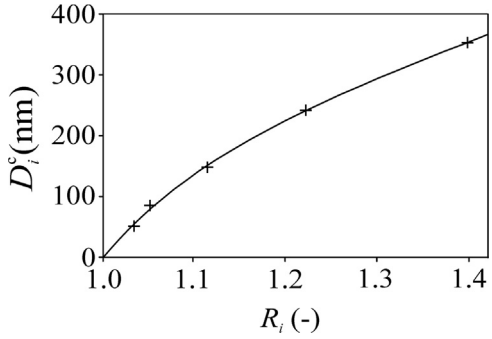

Fig. 2. Sigmoidal diameter calibration, $D_i^c(R_i)$, obtained from PS standards. Crosses indicate the measurement pairs $(R_p, \bar{D})$.

experiments. Standards of nominal diameters, 50 nm, 80 nm, 150 nm, 250 nm, 350 nm, were utilized for calibrating the CHDF according to the procedure detailed in Appendix B. For such purpose, the calibration standards were injected at concentrations of 1 mg/ml, and fractograms were obtained at a wavelength of 220 nm. The diameter calibration, $D_i^c(R_i)$, was obtained by fitting a sigmoidal function (whose exact mathematical expression is unknown since it is neither reported nor described by the CHDF manual) to points $(R_p, \bar{D})$, where R_p is the relative peak time of the fractogram $\tau_R(R_i)$ and $\bar{D}$ is the average diameter reported by the manufacturer (Table 1). The obtained calibration is presented in Fig. 2.

Three latex samples (L_1, L_2, L_3), were prepared on the basis of the PS standards of Table 1. L_1 was the standard of nominal diameter $D_{nom}=250$ nm. L_2 was a blend of three standards of $D_{nom}=200$ nm/250 nm/300 nm, in weight fractions of 25%/50%/25%, respectively. The corresponding number fractions are: 38.8%/46.8%/14.4%, which were calculated from data of Table 1, assuming Gaussian number PSDs. L_3 was a blend of two standards of $D_{nom}=150$ nm/300 nm, in weight fractions of 50%/50%, respectively (number fractions: 87.4%/12.6%). Note that the three latex samples were prepared with some of the PS standards utilized for calibrating the CHDF in order to ensure that all samples fall inside the range of the diameter calibration. L_2 was prepared to exhibit a PSD wider than that of L_1; while L_3 was prepared to obtain a bimodal PSD. All latexes were analyzed in order to evaluate the ability of the proposed method for estimating PSDs of different sizes, widths, and shapes. Additionally, the estimation of narrow modes normally present in the characterization of standards is an important challenge for CHDF.

Samples L_1, L_2, and L_3 were injected into the CHDF. The baseline-corrected multi-wavelength fractograms of Fig. 3 were obtained at discrete times from 0 to 900 sec with increments of 1 sec. From the measured fractograms, the PSD of each latex was estimated through the method described in the previous section. For such purpose, a GRNN with 4 inputs (the normalized T measurements at $\lambda_j=220$ nm, 240 nm, 260 nm, and 280 nm), 237 outputs (the ordinates of the instantaneous PSD, $\hat{f}_{i*}(D_n)$, at diameters from 10 to 600 nm with increments of 2.5 nm), and K=44,000 was implemented. The GRNN training was carried out through a set of $K_t=45{,}570$ patterns generated as follows: i) a PSD $f_k(D_n)$ (or $\mathbf{f}_k$) was generated on the basis of an exponentially modified Gaussian (EMG) distribution for given values of the average diameter ($\bar{D}_k$), standard deviation (σ_k), and decay constant of the exponential component (ν_k), as follows:

$$f_k(D_n) = \frac{\Delta D}{\sqrt{2\,\pi}\,\sigma_k} e^{\left[-\frac{(D_n-\bar{D}_k)^2}{2\,\sigma_k^2}\right]} * \frac{e^{(-D_n/\nu_k)}}{|\nu_k|/\Delta D} \tag{8}$$

where the symbol '*' stands for convolution product; and ii) the

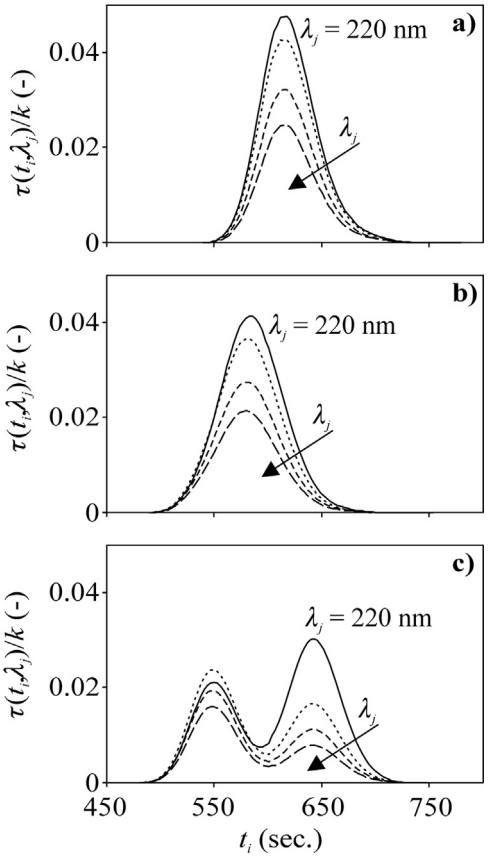

Fig. 3. Multi-wavelength fractograms $\tau(t_i, \lambda_j)/k$, with $k=\sum_{i=1}^{I}\tau(t_i, 220\text{nm})$, measured at $\lambda_j=220$ nm, 240 nm, 260 nm and 280 nm, for latex L_1 (a), L_2 (b), and L_3(c).

normalized T measurement $\tilde{\tau}_k(\lambda_j)$ (or $\tilde{\boldsymbol{\tau}}_k$) was calculated through Eq. (A.2) on the basis of $f_k(D_n)$, and adopting $c = 1$ (m^{-3}); water refractive index (since is the majority constituent of the carrier fluid in CHDF), $n_m(\lambda_j)=1.3869$, 1.3769, 1.3691, 1.3629 [31], and polystyrene refractive index, $n_p(\lambda_j)=2.1262+0.2122$ i, 1.8779+0.0046 i, 1.7804+0.0104 i, 1.7323+0.003 i [32], at $\lambda_j=220$ nm, 240 nm, 260 nm, and 280 nm, respectively. It is assumed that minority species, such as emulsifier, that may be present in the PS particles does not significantly modify the refractive index.

Steps i) and ii) were implemented for several values of $\bar{D}_k$, σ_k and ν_k in order to generate the set of 45,570 pairs $\{\tilde{\boldsymbol{\tau}}_k, \mathbf{f}_k\}$. For such purpose, $\bar{D}_k$ was varied from 10 nm to 550 nm at regular intervals of 2.5 nm; σ_k was varied from 1 nm to 10 nm at regular intervals of 1 nm; and ν_k was varied from −10 to 10 nm at regular intervals of 1 nm. The GRNN was trained by using K=44,000 randomly selected patterns. The remaining $K^*=1{,}570$ patterns were utilized for determining the smoothness parameter s_k through the Holdout method (see previous section), yielding $s_k=0.075$ ($k=1, \ldots, K$). The estimation algorithm was implemented in Matlab (MathWorks). The complete training procedure was carried out in approximately 600 seconds (in a standard personal computer equipped with 8 GB of RAM and an Intel(R) Core(TM) i3-4170 CPU). With the detailed GRNN architecture, the estimation of a single PSD takes approximately 0.05 sec. The choice of EMGs as base functions of the training pattern allows the approximation of a wide variety of distributions (e.g. Gaussian, normal-logarithmic, etc.).

For comparison purposes, the PSDs of latex L_1, L_2, and L_3 were also estimated through: i) a DLS equipment (Zetasizer Nano ZSP, from Malvern Instruments Ltd.), with a data treatment based on a regularized non-negative constrained least squares algorithm; and ii) the standard CHDF data treatment based on the fractogram

detected at 220 nm, the calibration of diameters of Fig. 2, and the procedure described in Appendix B.

Also for comparison, the number average diameter, $\bar{D}$, and the standard deviation, σ, of each estimated PSD were calculated as follows:

$$\bar{D} = \frac{\sum_{n=1}^{N} D_n \, f(D_n)}{\sum_{n=1}^{N} f(D_n)} \tag{9a}$$

$$\sigma = \left(\sum_{n=1}^{N} f(D_n)[D_n - \bar{D}]^2 \right)^{1/2} \tag{9b}$$

For the particular case of the bimodal PSD, $\bar{D}$, σ, and the weight fraction, w_f (%), were calculated separately for each mode. For calculating w_f, the weight PSD $w(D_n)$ was first calculated as: $w(D_n) = k_w \, D_n^3 \, f(D_n)$; where k_w is a normalization constant such that $\sum_{n=1}^{N} w(D_n) = 1$. Then, the weight fractions of both modes, $w_{f,1}$ and $w_{f,2}$, were calculated as $w_{f,1} = 100 \sum_{n=1}^{N*} w(D_n)$ and $w_{f,2} = 100 \sum_{n=N*+1}^{N} w(D_n)$, respectively; and N* was selected at the minimum between both estimated modes, and such values can vary according to the estimation method utilized.

4. Results

Fig. 4a and b show the average diameter $\bar{D}$ and the standard deviation σ (calculated through Eqs. (9a) and (9b), respectively) of all the instantaneous PSDs (estimated through the proposed method), and Fig. 4c shows the estimated instantaneous normalized concentration $\hat{c}(t_i)/C_T$ (obtained through Eq. (1), with $\lambda_j = 220$ nm), as a function of the elution time t_i. Fig. 5 shows the global estimated PSDs obtained with the proposed method, $\hat{f}_{pr}(D_n)$ (calculated through Eq. (2)), with the standard CHDF data treatment at single wavelength detection, $\hat{f}_{st}(D_n)$, and from DLS measurements, $\hat{f}_{DLS}(D_n)$. Table 2 compares the average diameter $\bar{D}$ and standard deviation σ of all estimated PSDs with the corresponding values reported by the manufacturer (obtained by DCP). For the bimodal PSD (latex L_3), Table 2 also compares the estimated weight fraction of each mode w_f with the known amounts used in its preparation.

From Fig. 4a and b, the estimated average diameters and standard deviations of the instantaneous PSDs of latex L_1 were almost constant along the elution time range. This result seems reasonable because L_1 is a narrow standard, and therefore the fractogram dispersion was mainly a consequence of the IB in the capillary. For this reason, all the instantaneous PSDs were quite similar. On the contrary, latexes L_2 and L_3 exhibited instantaneous $\bar{D}$ and σ that decrease with the elution time. The erratic estimates of $\bar{D}$ and σ at the extremes of the time elution range are due to a poor signal-to-noise ratio at the fractograms tails that deteriorates the PSD estimated with the neural network. Fortunately, these erratic estimates mainly occur at times where concentrations are low (see Fig. 4c), and therefore their impact on the final estimated PSDs is negligible.

In general, acceptable PSD estimates were obtained for all analyzed samples (Table 2), although some slight differences in $\bar{D}$ and σ with respect to DCP were observed. In particular, the proposed method was able to recover the expected number of PSD

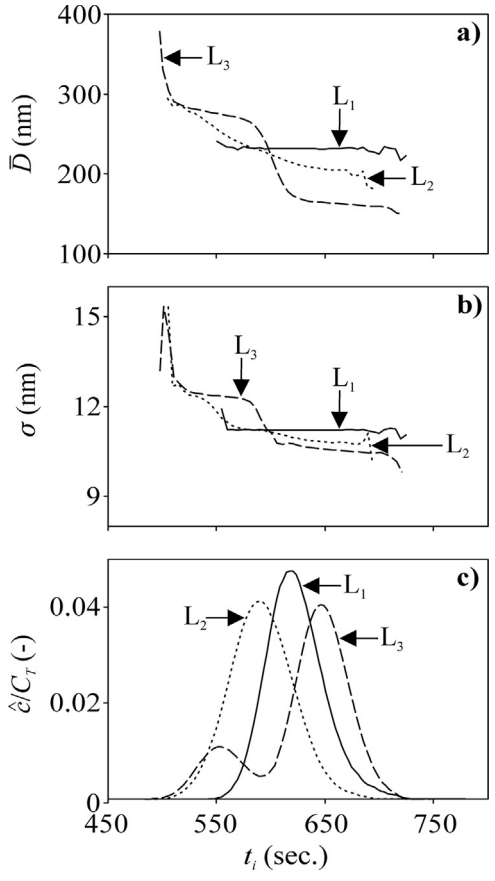

Fig. 4. a, b) Average diameter $\bar{D}$ and standard deviation σ of the estimated instantaneous PSDs obtained through the proposed method; c) Estimated instantaneous concentration $\hat{c}/C_T$.

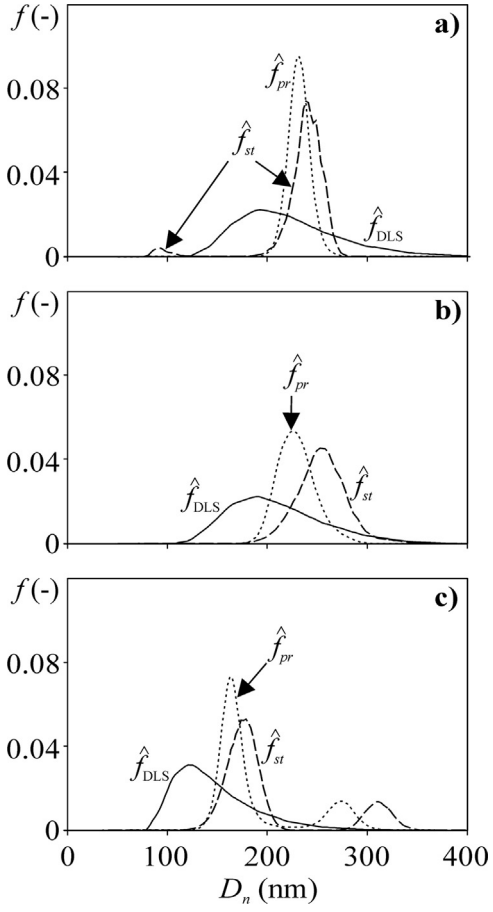

Fig. 5. Estimated PSDs through the proposed method ($\hat{f}_{pr}$), the standard data treatment ($\hat{f}_{st}$), and DLS ($\hat{f}_{DLS}$), for latex L_1 (a), L_2 (b), and L_3 (c).

Table 2
Number average diameters, $\bar{D}$ [nm], and standard deviations, σ [nm], of the estimated PSDs obtained by DCP (provided by Polysciences, Inc.), DLS, standard CHDF, and the proposed data treatment. For the bimodal PSD the estimated weight fraction, w_f (%), of each mode is also shown (true value 50% for both $L_{3,1}$ and $L_{3,2}$).

			DCP	DLS	Standard CHDF	Proposed method
L_1		$\bar{D}$	244	221	239	234
		σ	8.9	51.0	14.3	11.5
L_2		$\bar{D}$	235[a]	212	255	235
		σ	29.1[a]	50.7	25.0	20.7
L_3	Mode 1	$\bar{D}$	150	147	175	166
		σ	8.9	40.8	15.7	13.7
		w_f	50[b]	100	44.2	47.5
	Mode 2	$\bar{D}$	286	-[c]	311	272
		σ	19.5		13.7	16.3
		w_f	50[b]		55.8	52.5

[a] values estimated on the basis of $\bar{D}$ and σ corresponding to each standard in the blend, assuming Gaussian number PSDs.
[b] values utilized in the preparation of latex L_3.
[c] only one mode was estimated.

modes (see Fig. 5), and also the average diameters and the standard deviations of all PSDs (including both modes in latex L_3) (see Table 2). Additionally, the proposed method accurately estimates the weight fractions of both modes in L_3. In contrast, although acceptable estimates of average diameters and standard deviations were obtained for sample L_2, the method was incapable of discriminating between the three modes, and the estimated PSD was unimodal. This result seems reasonable since the average diameters of all modes in L_2 were relatively close. On the other hand, the standard CHDF data treatment produced erratic PSDs when compared with DCP estimates. For example, for latex L_1, the estimated $\bar{D}$ was close to that obtained by DCP. This result was expected because L_1 was utilized as a calibration standard for obtaining the calibration curve of Fig. 2. The estimated PSD of latex L_2 produced a standard deviation close to the DCP value, but exhibited only one mode with an erroneous average diameter (approximately 10% greater than DCP). Also, both modes of L_3 exhibited overestimated average diameters (with percentage errors close to 10%). Besides, the estimated PSDs of L_1 exhibited an erroneous peak of weight fraction smaller than 1% and an average diameter near 100 nm. This erroneous peak can be due to the methodology used for correcting the IB, which is based on the Ishige' method, that normally produces erroneous peaks in the estimated PSDs when the IB function is not accurately known [17,33]. Finally, note the low resolution of the PSDs estimated by DLS. Particularly, L_3 were erroneously estimated as a unimodal PSD. Additionally, all PSDs obtained by DLS exhibited an underestimated average diameter and an overestimated standard deviation. In order to corroborate these estimates, all DLS measurements were repeated with a Nanosizer equipment (from Malvern Instruments Ltd.), and similar results to those of Table 2 were obtained. This is a typical result when estimation is carried out through single angle DLS [1,21]. Also, the large overestimated widths of the PSDs obtained by DLS can be a consequence of excessive regularizations in the implemented non-negative constrained least squares [15].

In order to evaluate the repeatability and robustness of the proposed method, sample L_2 was sequentially injected four times. In the first two injections, the wavelengths were 220 nm, 240 nm, 260 nm, and 280 nm; in the other two injections, the selected wavelengths were 230 nm, 250 nm, 270 nm, and 290 nm. For these last two experiments, a new GRNN training was made with their corresponding refractive indexes: $n_m(\lambda_j)=1.3816$, 1.3727, 1.3658, 1.3602 [31], and $n_p(\lambda_j)=1.9931+0.269$ i; $1.7985+0.0080$ i; $1.7408+0.0083$ i; $1.7323+0.000$ i [32]; at $\lambda_j=230$ nm, 250 nm, 270 nm, and 290 nm, respectively. Fig. 6 presents the estimated PSDs; all PSDs are quite similar, thus suggesting an acceptable repeatability of the method as well as a reasonable robustness under changes of the selected wavelengths.

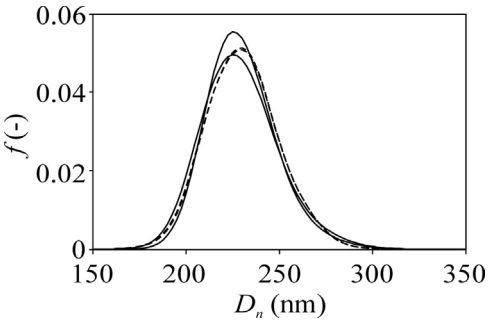

Fig. 6. PSD estimates corresponding to four sequential injections of latex L_2: 2 experiments carried out at $\lambda_j=220$ nm, 240 nm, 260 nm and 280 nm (—); and 2 experiments carried out at $\lambda_j = 230$ nm, 250 nm, 270 nm, and 290 nm (- -).

Even though not shown, the proposed method was also applied to samples based on the standards of 50 nm and 80 nm, and larger estimation errors were observed. This behavior seems to be reasonable because, at smaller sizes, the information on the PSD contained in the T measurements decreases [1]. In principle, for smaller particles, the proposed method could be extended by using a larger number of wavelengths; however this extension must be further investigated.

5. Conclusions

A novel procedure for estimating the PSD of latex from multi-wavelength CHDF measurements has been proposed and critically assessed on the basis of samples with PSDs of different sizes and shapes. The method is easy to be implemented and automated, and does not require calibration nor correction for IB, thus avoiding the negative effects of uncertainties in the estimated calibration and IB function which may produce meaningful errors in the estimated PSDs [18]. Additionally, the new methodology avoids the utilization of the marker injection. However, it requires the training of the neural network with artificial data for each polymer analyzed.

In general, the new method was able to acceptably recover the average diameters and the standard deviations of the estimated PSDs. In the bimodal sample, the weight fractions of each mode were acceptably estimated. The new method showed a high repeatability when samples were analyzed several times and at different detection wavelengths. Also, when compared to estimates obtained by DLS and the standard CHDF data treatment, the proposed method appears to produce more accurate estimates.

As a drawback, the proposed methodology requires the knowledge of the PRI at the detection wavelengths, which is also required in the standard CHDF data treatment. For example, in the analysis of latex L_2, an increment of 2.5% of the value of the refractive index utilized for training the GRNN produced a decrease of 9% in the average diameter of the estimated PSD. Unfortunately, the PRI is only known for a few polymers; and for copolymers the problem can be even worse.

The present approach, which is based on the increase of information content on the PSD when employing multi-wavelength

UV detection, could also be extended to any fractionation technique with turbidity detection (such as, FFF, DCP, and HDC).

Acknowledgements

L.A.C., J.R.V., and L.M.G. are grateful for the financial support received from CONICET (PIP 112-201101-00359), Universidad Nacional del Litoral (CAI+D 2011, 501-201101-00050 LI) and Universidad Tecnológica Nacional (Argentina) (PID ENUTIFE0002405TC). J.R.L. and M.A. acknowledge the financial support from the Basque Government (GV-IT-303-10), Ministerio de Economía y Competitividad (MINECO, Ref. CTQ2014-59016P), Gipuzkoako Foru Aldundia (EXP/55/14) and UPV/EHU (UFI 11/56). M. A. specially acknowledges the financial support obtained through the Post-doctoral fellowship Juan de la Cierva en Formación (FJCI-2014–22336), from the Ministry of Economy and Competitiveness of Spain.

Appendix A. Mathematical model of turbidity measurements

The T measurement carried out at the "in vacuum" UV–vis wavelengths λ_j, $\tau(\lambda_j)$ ($j = 1, \ldots, J$), is defined as:

$$\tau(\lambda_j) = \frac{1}{\ell} \ln\left[I_0(\lambda_j)/I_t(\lambda_j) \right] \tag{A.1}$$

where ℓ is the optical path length, $I_0(\lambda_j)$ is the incident beam intensity and $I_t(\lambda_j)$ is the emerging beam intensity (measured in the direction of the incident beam) [1]. Then, $\tau(\lambda_j)$ is related to the PSD $f(D_n)$ through the following linear mathematical model:

$$\tau(\lambda_j) = (\pi/4)\ c \sum_{n=1}^{N} Q_{ext}[D_n, \lambda_j, n_m(\lambda_j), n_p(\lambda_j)]\ \ D_n^2\ f(D_n) \tag{A.2}$$

where c is the particle number concentration in the detector cell; and $Q_{ext}[D_n, \lambda_j, n_m(\lambda_j), n_p(\lambda_j)]$ is calculated through the Mie scattering theory and represents the light extinction efficiency at λ_j of a particle of diameter D_n and refractive index $n_p(\lambda_j)$ immersed in an homogeneous and non-absorbing medium of refractive index $n_m(\lambda_j)$[13].

The estimation of the PSD $f(D_n)$ through $\tau(\lambda_j)$ (j=1, …, J) involves solving the standard inverse problem of Eq. (A.2). Since concentration c is a-priori unknown, then Eq. (A.2) is inverted for estimating the scaled version of $f(D_n)$, i.e., $f^*(D_n) = c\ f(D_n)$. Finally, the PSD $f(D_n)$ is obtained after normalizing $f^*(D_n)$, as follows:

$$f(D_n) = f^*(D_n) / \sum_{n=1}^{N} f^*(D_n) \tag{A.3}$$

Appendix B. PSD estimate by standard CHDF

The classical CHDF measurement, $\tau(t_i)$, represents an UV–vis signal (or a turbidity signal) taken at a single wavelength λ_0, as a function of the elution time t_i. Following DosRamos and Silebi [17], one can define the relative elution time, R_i, as:

$$R_i = t_m/t_i \tag{B.1}$$

where t_m is the elution time of the marker [17]. Then, the R_i-based fractogram, $\tau_R(R_i)$, is related to $\tau(t_i)$, as follows:

$$\tau_R(R_i) = \tau(t_i)\frac{1}{|dR_i/dt_i|} = \tau(t_i)\frac{1}{t_m/t_i^2} \tag{B.2}$$

where the factor $|dR_i/dt_i| = (t_m/t_i^2)$ corrects the ordinates of $\tau(t_i)$ due to the non-linear transformation of Eq. (B.1).

A usual procedure for obtaining the diameter calibration curve, $D_i^c(R_i)$, involves the injection of P narrow standards of known diameters $\bar{D}_p$ ($p = 1, \ldots, P$). Then, the relative elution times $R_p = t_m/t_p$ are assigned at the peaks of the fractograms; and $D_i^c(R_i)$ is obtained by fitting the pairs $\{\bar{D}_p, R_p\}$ with a known function (typically, a polynomial or a sigmoidal function).

The PSD ordinates, $f(D_i^c)$, are related to $\tau_R(R_i)$ as follows [16,17]:

$$f(D_i^c) \propto \frac{\tau_R(R_i)}{(\pi/4)\ Q_{ext}[D_i^c(R_i), \lambda_0, n_m(\lambda_0), n_p(\lambda_0)]\ D_i^c(R_i)^2} \frac{1}{\frac{dD_i^c(R_i)}{dR_i}} \tag{B.3}$$

where $dD_i^c(R_i)/dR_i$ is used to correct the ordinates of $\tau_R(R_i)$ for the non-linear transformation involved in the first factor of the right hand side of Eq. (B.3). Then, $f(D_i^c)$ can be transformed to an equivalent PSD, $f^*(D_n)$, in a different diameter axis (D_n), through an interpolation procedure. Finally, $f^*(D_n)$ can be normalized through Eq. (A.3) to obtain the PSD $f(D_n)$.

The IB is an important cause of imperfect resolution in CHDF, and can strongly affect the estimation of narrow PSDs or multimodal distributions with narrow modes. The IB is a consequence of the finite injection volume and detection cell volume, the non-uniform parabolic velocity profile in the capillary, and the Brownian motion of the particles that affects their axial displacements. To correct for IB, the method proposed by Ishige et al. [33] is normally applied to the measured fractogram $\tau(t_i)$ (previous to the data treatment of Eqs. (B.1) to (B.3)) thus obtaining more accurate PSD estimates [17].

References

[1] Gugliotta LM, Clementi LA, Vega JR. Particle size distribution. main definitions and measurement techniques. In: Gugliotta LM, Vega JR, editors. Measurement of particle size distribution of polymer latexes. Kerala, India: Research Signpost – Transworld Research Network; 2010 [Ch. 1].
[2] Gugliotta LM, Vega JR, Meira GR. Latex Particle Size Distribution by Dynamic Light Scattering: computer Evaluation of Two Alternative Calculation Paths. J Coll Int Sci 2000;228:14–17.
[3] Vega JR, Gugliotta LM, Gonzalez VDG, Meira GR. Latex particle size distribution by dynamic light scattering: novel data processing for multiangle measurements. J Coll Int Sci 2003;261:74–81.
[4] Gugliotta LM, Stegmayer GS, Clementi LA, Gonzalez VDG, Minari RJ, Leiza JR, et al. A neural network model for estimaing the particle size distribution of dilute latex from multiangle dynamic light scattering measurement. Part Par Syst Charact 2009;26:41–52.
[5] Liu X, Shen J, Thomas JC, Clementi LA, Sun X. Multiangle Dynamic light scattering using a modified chahine method. J Quant Spectrosc Radiat Transf 2012;113(6):489–497.
[6] Li L, Yang K, Li W, Wang W, Guo W, Xia M. A recursive regularization algorithm for estimating the particle size distribution from multiangle dynamic light scattering measurements. J Quant Spectrosc Radiat Transf 2016;178:244–254.
[7] Renliang X. Light scattering: a review of particle characterization applications. Particuology 2015;18:11–21.
[8] Mroczka J, Szczuczynski D. Improved technique of retrieving particle size distribution from angular scattering measurements. J Quant Spectrosc Radiat Transf 2013;129:48–59.
[9] Clementi LA, Vega JR, Gugliotta LM, Quirantes A. Characterization of spherical core-shell particles by static light scattering. Estimation of the core- and particle size distribution. J Quant Spectrosc Radiat Transf 2012;113(17):2255–2264.
[10] Eliçabe G, Garcia-Rubio L. Latex particle size distribution from turbidimetry using inversion techniques. J Coll Int Sci 1989;129(1):192–200.
[11] Eliçabe G, Frontini G. Determination of the particle size distribution of latex using a combination of elastic light scattering and turbidimetry: a simulation study. J Coll Int Sci 1996;181:669–672.
[12] Llosent MA, Gugliotta LM, Meira GR. Particle size distribution of sbr and nbr latexes by UV–vis. turbidimetry near the rayleigh region. Rubber Chem Tech 1996;69:696–712.
[13] Vega JR, Frontini GL, Gugliotta LM, Eliçabe GE. Particle size distribution by combined elastic light scattering and turbidity measurements. A novel method to estimate the required normalization factor. Part Part Syst Charact 2003;20:361–369.
[14] Tang H, Lin JZ. Retrieval of spheroid particle size distribution from spectral extinction data in the independent mode using PCA approach. J Quant Spectrosc Radiat Transf 2012;115:78–92.
[15] Aster R, Borchers B, Thurber C. Parameter estimation and inverse problems.

USA: John Wiley & Sons; 2005.
[16] Silebi CA, DosRamos JG. Separation of submicrometer particles by capillary hydrodynamic fractionation (CHDF). J Coll Int Sci 1989;*130*:14–24.
[17] DosRamos JG, Silebi CA. The determination of particle size distribution of submicrometer particles by capillary hydrodynamic fractionation (CHDF). J Coll Interf Sci 1990;135:165–177.
[18] Clementi LA, Artetxe Z, Aguirreurreta Z, Agirre A, Leiza JR, Gugliotta LM, et al. Capillary hydrodynamic fractionation of hydrophobic colloids: errors in the estimated particle size distribution. Particuology 2014;*17*:97–105.
[19] Miller CM, Venkatesan J, Silebi CA, Sudol ED, El-Aasser MS. Characterization of miniemulsion droplet size and stability using capillary hydrodynamic fractionation. J Coll Int Sci 1994;162:11–18.
[20] Miller CM, Sudol ED, Silebi CA, El-Aasser MS. Capillary hydrodynamic fractionation (CHDF) as a tool for monitoring the evolution of the particle size distribution during miniemulsion polymerization. J Coll Int Sci 1995;172:249–256.
[21] Elizalde O, Leal P, Leiza JR. Particle size distribution measurements: a comparison of four commercial techniques. Part Part Syst Charact 2000;17:236–243.
[22] Erdem B, Sully Y, Sudol ED, Dimonie VL, El-Aasser MS. Determination of miniemulsion droplet size by sop titration. Langmuir 2000;16:4890–4895.
[23] Jung KT, Shul YG. Capillary hydrodynamic fractionation studies on the crystal growth of TS-1 Zeolite. J Non-Cryst Solids 2003;316:246–254.
[24] Mariz IDFA, De La Cal JC, Leiza JR. Synthesis of high solids content latexes with low viscosities and low particle sizes. Polymer 2010;51:4044–4052.
[25] Mariz IDFA, De La Cal JC, Leiza JR. Competitive particle growth: a tool to control the particle size distribution for the synthesis of high solids content low viscosity latexes. Chem Eng J 2011;168:938–946.
[26] Mariz IDFA. High solids content low viscosity latexes with small particle size [Ph.D. Thesis]. Donostia: University of the Basque Country; 2011.
[27] Casey MB, Sudol ED, El-Aasser MS. Evolution of droplet size distribution and composition in miniemulsions. J Polym Sci Part A: Polym Chem 2014;52:1529–1544.
[28] Picchio ML, Minari RJ, Gonzalez VDG, Passeggi MCG, Vega JR, Barandiaran MJ, et al. Waterborne acrylic-casein nanoparticles. Nucleation and grafting. Macromol Symp 2014;344:76–85.
[29] Haykin S. Neural networks: a comprehensive foundation.New Jersey, USA: Prentice Hall; 1999.
[30] Specht DF. A general regression neural network. IEEE Trans Neural Netw 1991;2(6):568–576.
[31] Bohren CF, Huffman DH. Absorption and scattering of light by small particles. New York, USA: John Wiley & Sons; 1983.
[32] Inagaki T, Arakawa ET, Hamm RN, Williams MW. Optical properties of polystyrene from the near infrared to the x-ray region and convergence of optical sum rules. Phys Rev B 1977;15:3243–3253.
[33] Ishige T, Lee SI, Hamielec HE. Solution of Tung's axial dispersion equation by numerical techniques. J Appl Polym Sci 1971;15:1607–1622.